Check for updates

RESEARCH ARTICLE

ADVANCED MATERIALS INTERFACES Open Access

www.advmatinterfaces.de

2D Halide Perovskite Phase Formation Dynamics and Their Regulation by Co-Additives for Efficient Solar Cells

*Min Liu, Daming Zheng, Tao Zhu, Karol Vegso, Peter Siffalovic, and Thierry Pauporté**

The incorporation of large organic ammonium ions renders the crystallization dynamics and layer formation process of halide perovskites complex, difficult to control, and leads to problems of suppressed charge transport with the formation of tiny-sized grains. In this paper, the use of methylammonium chloride (MACl) and an excess of PbI_2 is introduced as a co-additives in the precursor solution for the control of phenylmethylammonium or benzylammonium (PMA^+ spacer) and formamidinium (FA^+)-based quasi-2D $PMA_2FA_{n-1}Pb_nI_{3n+1}$ ($n = 5$) perovskite layers formation. By this method, the morphology of the layer, the inner phase distribution, and the charge transport properties are improved. By employing glow discharge-optical emission spectroscopy (GD-OES) and other techniques, it is revealed that the quasi-2D perovskites prepared in the presence of co-additives exhibit uniform removal dynamics of the solvent across the film. Furthermore, the grain growth mode, upon thermal annealing, is lateral. It results in large, monolithic grains with low-trap state density and excellent substrate coverage. Particularly, co-additives improve the cations dispersion upon the crystallization process, thus suppressing the low-n phase formed through the aggregation of spacer cations and accelerating the formation of the high-n phase.

1. Introduction

Perovskite solar cells (PSCs) have become a popular photovoltaic technology due to their high energy conversion efficiency and low processing cost.[1] For their commercialization, their present rather low stability remains a serious issue.[2] The stability of metal halide perovskite films can be enhanced by employing perovskites with lower dimensionality as an overlayer or at the grain boundaries.[3] Halide perovskites, with crystal structure stabilized by monoammonium (A′) or diammonium (A″) organic cation spacers, can also be directly employed as the solar light absorber.[4] Rudlesden–Popper (RP) and Dion–Jacobson (DJ) phases, with molecular formulas $A'_2A_{n-1}B_nX_{3n+1}$ and $A''A_{n-1}B_nX_{3n+1}$ (with A being a monovalent cation, B being Pb^{2+} or Sn^{2+} and X a halogen), respectively, are the two main types of perovskite structures with 2D perovskite-like slabs interleaved by A′ or A″ cation spacers.[5] In the following, we will use the term quasi-2D perovskite for the compounds with $2 \leq n \leq 5$. RP-phase perovskites are known to have an outstanding resistance capability against humidity.[6]

Although 2D/quasi-2D RP perovskites have numerous merits, several points remain to be solved for their efficient application in solar cells.[6b,7] For example, their quantum-well structure limits the charge carrier transport and increases charge carriers recombination due to the insulating feature of the A' organic cations.[8] Furthermore, owing to the huge spatial site resistance of organic spacer cations, their incorporation complicates the crystallization process of perovskite and renders the morphology of the layer challenging to control. It aggravates the non-radiative charge carrier recombination in quasi-2D-RP perovskite films and affects the photoelectric capability of perovskite solar cells.[9] Hence, various approaches have been developed to adjust the crystal growth orientation, such as hot-casting deposition, solvent engineering, and additive engineering. They aim at favoring a (111)/(101) crystal orientation to accelerate charge transport in quasi-2D RP perovskite devices.[10,11] Controlling the phase distribution and the growth direction of the perovskite layer is proposed as a promising strategy to enhance the charge transport of quasi-2D perovskites.[12] For example, Shao and co-workers introduced formamidinum (FA^+) cations to replace methylammonium (MA^+). It greatly increased the portion of the high-*n* phase, extraordinarily accelerated charge transport, and

M. Liu, D. Zheng, T. Zhu[+], T. Pauporté
Chimie ParisTech
PSL Research University
CNRS
Institut de Recherche de Chimie Paris (IRCP)
UMR8247, 11 rue P. et M. Curie, Paris F-75005, France
E-mail: thierry.pauporte@chimieparisrech.psl.eu

K. Vegso, P. Siffalovic
Institute of Physics
Slovak Academy of Sciences
Dubravska cesta 9, Bratislava 84511, Slovakia

K. Vegso, P. Siffalovic
Center for Advanced Materials and Applications (CEMEA)
Slovak Academy of Sciences
Dubravska cesta 5807/9, Bratislava 84511, Slovakia

The ORCID identification number(s) for the author(s) of this article can be found under https://doi.org/10.1002/admi.202300773

[+]Present address: Department of Electrical and Electronic Engineering, The Hong Kong Polytechnic University, Hung Hom, Kowloon, Hong Kong 999 077, China

© 2023 The Authors. Advanced Materials Interfaces published by Wiley-VCH GmbH. This is an open access article under the terms of the Creative Commons Attribution License, which permits use, distribution and reproduction in any medium, provided the original work is properly cited.

DOI: 10.1002/admi.202300773

stabilized quasi-2D PSC.[13] Kong et al. introduced an additive approach to rebuild quasi-2D perovskite architectures through the interaction between the robust hydrogen bonding of methane sulfonates and butyl ammonium (BA^+) cations, resulting in enhanced energy acceptor–donor ratio of quasi-2D perovskite layers and ameliorated charge transport.[14] Huang's team designed an intermediate perovskite phase to homogenize the phase distribution by employing molten salt spacer n-butylamine acetate into the precursor solution. It led to an enhanced photoelectric capability of the PSC with a power conversion efficiency (*PCE*) of 16.25%.[15] In the literature, only single additive approaches have been described to promote the phase distribution of 2D perovskites and to enhance the charge carrier transport. However, these approaches still have some limitations in promoting layer crystallization and controlling layer morphology.

The first embodiments of Rudlesden—Popper (RP) type low-dimensional organic–inorganic perovskite solar cells were demonstrated by employing phenylethylammonium (PEA^+) in 3D $MAPbI_3$, transforming the 3D architecture into 2D $(PEA)_2(MA)_2Pb_3I_{10}$.[16] In contrast to these well-known MA-based 2D perovskites, FA-based perovskites, which are assumed to be more stable phases under severe environmental and operational conditions,[17] remain underrepresented to date. This is likely due to the necessity of stabilizing FA-based systems with another monovalent cation and to the difficulty in obtaining high-quality FA-based perovskite layers in contrast to MA-based systems.[18]

In this paper, a co-additive approach is adopted to manufacture $n = 5$ (quasi-2D), FA-based films of perovskites with homogeneous phase distribution and enhanced crystal quality. We show that methylammonium chloride (MACl) and lead iodide (PbI_2) co-additives accelerate the confined crystallization and the phase rearrangement in quasi-2D perovskites, which can ameliorate the dispersion of spacer cations and of FA^+ upon the recrystallization process. It therefore suppresses the formation of low-n phases induced through the aggregation of spacer cations and promotes the formation of higher-n phases. Moreover, we show by glow-discharge optical emission spectroscopy (GD-OES) that a co-additive approach changes the growing direction of the perovskite layer upon annealing, improving the overall crystallization quality and layer homogeneity. Hence, this approach is proven to improve the phase distribution within quasi-2D perovskite and to be beneficial to charge carrier transport. The corresponding perovskite solar cells efficiencies increased by more than 500% with co-additive compared to pristine PSCs. The solar cell's *PCE* and stability were substantially enhanced. The best *PCE* reached 17.71%, which is one of the highest efficiency of any low-dimensional PMA-based (with PMA^+ being phenylmethylammonium or benzylammonium) perovskite solar cells with $n \leq 6$ reported up to now.

2. Results and Discussion

2.1. Effect of Co-Additives on the Film Properties

We manufactured FA-based 2D-RP perovskite ($n = 5$) layers via one-step sequential deposition, as demonstrated in **Figure 1a**. A perovskite precursor film was first deposited on the TiO_2 electron transport layer (ETL) by spin-coating a solution, dripped with anti-solvent, and subsequently thermally annealed at 150 °C for 14 min. Perovskite layers were prepared from a solution containing PMAI : FAI : PbI_2 (FAI = formamidinium iodide; PMAI = phenylmethylammonium iodide; PbI_2 = lead iodide) at a PbI_2 concentration of 1.3 mol L^{-1} and with molar ratios of 2 : 4 : 5 that corresponds to a $PMA_2FA_4Pb_5I_{16}$ general formula. We also investigated precursor solutions with an addition of 40% MACl and with 40% MACl plus 20% PbI_2 excess to manufacture perovskite layers. For convenience, the samples with the addition of 0% MACl, 40% MACl, and 40% MACl with 20%PbI_2 are referred to as "Pristine", "MC" and "MC&PI", respectively, in the following. As shown in Tables S1–S3 (Supporting Information), investigating different concentrations of MACl and PbI_2, led to best results for the additive with 40% MACl and 20% PbI_2.

Scanning electron microscopy (SEM) observations were used to study the changes in surface morphology of pristine and modified FA-based RP 2D perovskite layers. As shown in Figure S1 (Supporting Information), the pristine sample exhibited poor surface uniformity with a rough surface, numerous obvious cracks, and pronounced pinholes that are responsible to some extent for the low V_{OC} of the cell. The cross-sectional SEM image of the pristine sample in Figure 1b shows no clear grain boundaries along the vertical direction in the layer. The MC perovskite layers show numerous compact and homogeneous grains, grain interstitials are clearly visible. After the addition of MACl, a dense perovskite layer with moderate grain size was formed. Increasing the concentration of the MACl additive resulted in an increase in grain size, as shown in Figure S2 (Supporting Information). MACl effectively stabilizes a high-n phase intermediate by cationic site substitution alone, resulting in a highly crystalline high-n phase perovskite with an ultra-pure phase.[19] Nevertheless, several vertical crystal boundaries are evident within the layer, possibly formed by high-n perovskite grains. The distinctive horizontal grain boundaries might be caused by residual stresses due to broken low-n/high-n perovskite grains.[20] The cross-sectional SEM picture (Figure 1b) shows no clear vertical orientation of grain boundaries. To solve this issue, MC&PI approach was utilized. The addition of PbI_2 substantially suppresses the aggregation of colloids, which could enhance the crystallization process, leading to the generation of a quasi-2D perovskite layer and increasing the size of grains.[21] After employing PbI_2 excess, the MC&PI layer exhibited a dense and smooth surface morphology. This crystal morphology could be better identified by the cross-sectional SEM. Compared to the pristine perovskite layer with disordered crystals, the grain quality of perovskite layers was substantially enhanced after using MC&PI co-additives. Furthermore, MC&PI perovskite presents a columnar monolithic structure, that is benefitial for the charge transport and should enhance the short-circuit current density (J_{sc}).[22]

To further explore the effect of MC&PI on the crystallinity and orientation of quasi-2D perovskite, grazing-incidence small-angle X-ray scattering (GIWAXS) of the perovskite layers is shown in Figure 1c. The GIWAXS pattern of the pristine sample reveals a textured layer with two distinct orientations, one of which is the more favorable, with the vertical orientations of 2D perovskite slabs indicated by a 111 maximum along the q_z direction.[23] Just the addition of MACl alone improves the texture significantly and the MC sample shows an uniaxial texture with the (111) planes parallel to the sample surface, as indicated

© 2023 The Authors. Advanced Materials Interfaces published by Wiley-VCH GmbH

21967350, 2024, 6, Downloaded from https://onlinelibrary.wiley.com/doi/10.1002/admi.202300773 by HONG KONG POLYTECHNIC UNIVERSITY HUNG HOM, Wiley Online Library on [26/11/2024]. See the Terms and Conditions (https://onlinelibrary.wiley.com/terms-and-conditions) on Wiley Online Library for rules of use; OA articles are governed by the applicable Creative Commons License

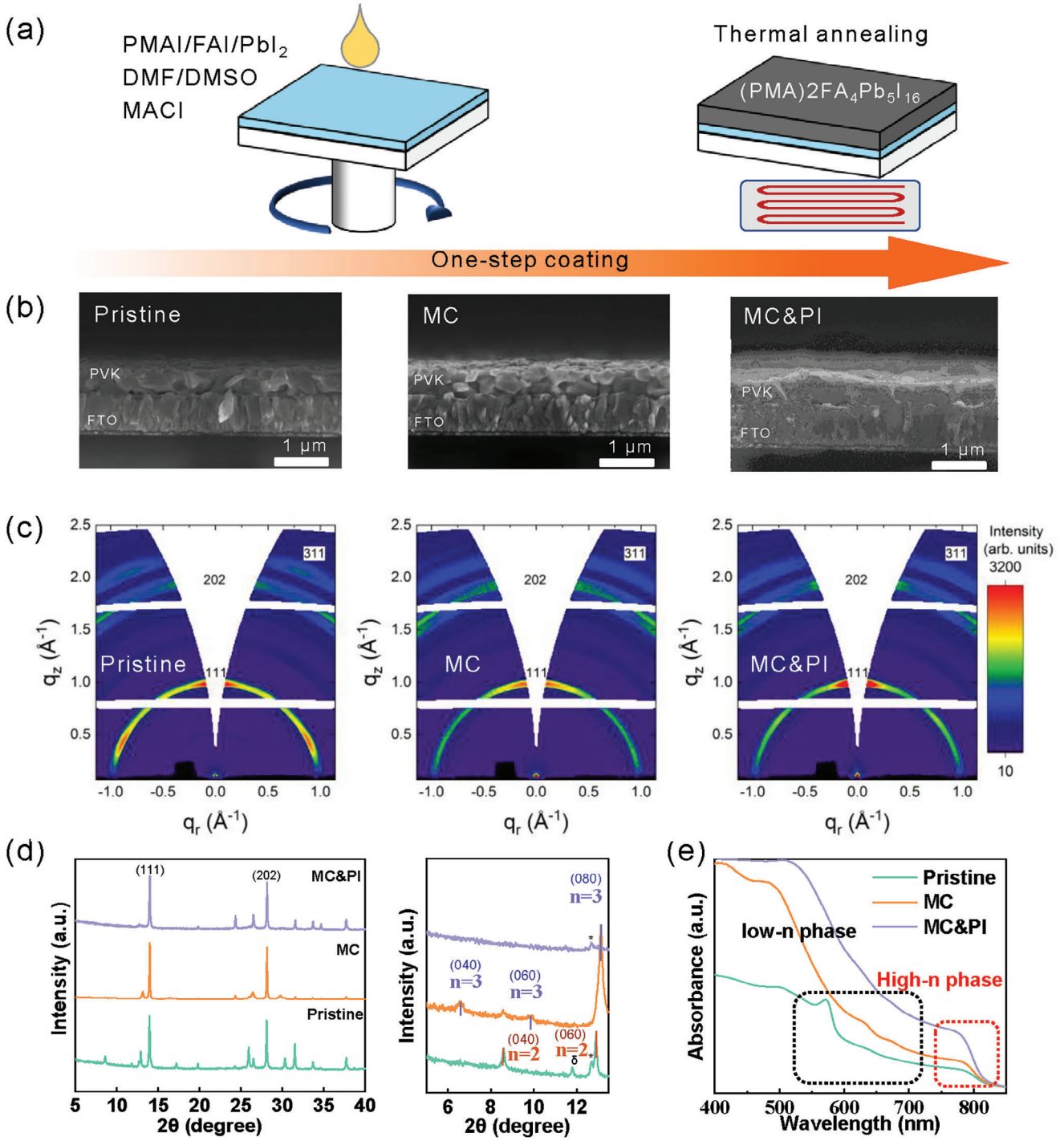

Figure 1. a) Schematic of the manufacturing process of FA-based 2D-RP perovskite solar cells applying the one-step sequential procedure. b) Cross-sectional scanning electron microscopy (SEM) images for the pristine, MC, and MC&PI films. c) GIWAXS patterns of the pristine, MC, and MC&PI films. d) X-ray diffraction (XRD) patterns of the pristine, MC, and MC&PI film. The δ and * labels indicate the δ-$FAPbI_3$ and PbI_2 phases, respectively. e) UV–vis absorption spectra of the pristine, MC, and MC&PI films.

by a single maximum along the q_z direction.[23b] The combined effect of MC&PI additives further improves the texture, as indicated by the increased intensity of 111 diffraction compared to the MC additive alone. Meaning that MC&PI promotes an enhanced vertical alignment of 2D perovskite layers, which is beneficial for charge transport through the layer. Additional information on perovskite phases can be found in conventional θ–2θ XRD scans (Figure 1d), supplementing the information in the missing wedge of GIWAXS patterns. For reference purposes, XRD scans of perovskite layers with $n = 1/2/3$ are shown in Figure S3

© 2023 The Authors. Advanced Materials Interfaces published by Wiley-VCH GmbH

21967350, 2024, 6, Downloaded from https://onlinelibrary.wiley.com/doi/10.1002/admi.202300773 by HONG KONG POLYTECHNIC UNIVERSITY HUNG HOM, Wiley Online Library on [26/11/2024]. See the Terms and Conditions (https://onlinelibrary.wiley.com/terms-and-conditions) on Wiley Online Library for rules of use; OA articles are governed by the applicable Creative Commons License

(Supporting Information). The parasitic PbI_2 phase was low, especially in the presence of the 20% PbI_2 excess. The XRD pattern of the pristine sample exhibited 2D $n = 2$ phase peaks and a small amount of undesired δ-phase. When MACl was added at 40 mol%, the $n = 3$ phase was present, and the $n = 2$ phase decreased slightly. As previously reported, MACl improves the layer morphology and phase crystallinity, which directly affects the enhancement of charge transport in the perovskite layer.[19] Finally, for the perovskite layer with MC&PI additives, the peaks for $n = 3$ phase are missing, indirectly confirming the vertical orientation of the perovskite layers already validated by GIWAXS measurements.

The UV–vis absorption spectra of pristine, MC, and MC&PI FA-based quasi-2D perovskite layers ($n = 5$) and their differential absorption spectra are shown in Figure 1e and Figure S4b (Supporting Information), respectively. Figure S4a (Supporting Information) exhibits the UV–vis absorption spectra of reference $n = 1/2/3$ perovskite layers. It can be seen that there are two clear excitonic peaks corresponding to a distribution of perovskite phases with low-n phase ($n = 2$) and high-n phase for pristine quasi-2D perovskite layers, demonstrating the existence of multiple perovskite phases in the pristine layers. For the MC layer, a weak ($n = 3$) absorption peak is evident, indicating the generation of a higher n phase through MC. Furthermore, the absorption of the MC layer is improved, which may be assigned to the transformation from the low-n phase (defined as n lower than four) to the high-n phase (defined as n higher than four).[24] Likewise, for the MC&PI layer, there was no clear absorption peak in the short-wavelength range and the absorption intensity of the MC&PI layer was enhanced. This phenomenon could be attributed to the increase and homogenization of n phases induced by MC&PI in the quasi-2D perovskite layer, implying that the MC&PI promotes the generation of high-n phases, leading to a stronger absorption of the quasi-2D perovskite layer. It is because MC&PI substantially suppresses the aggregation of colloids in the precursor solution and thus improves the recrystallization upon the annealing process.[21] The clustered 2D phases vanish and PMA^+ spreads evenly across the perovskite film, resulting in the disappearance of the low-n phases and the concurrent rise of the high-n phases observed during characterization.[8] The abundant high-n phases in MC&PI quasi-2D perovskite layers provide exceptional pathways for charge carrier extraction, consequently leading to increased J_{sc} (short-circuit current) in quasi-2D PSCs.[25] Tauc plots of 3D (1.525 eV) and MC&PI (1.527 eV) layers are shown in Figure S4c,d (Supporting Information).

2.2. Investigation of Film Formation Process

To acquire an extensive insights into the nucleation and growth mechanism of various perovskite phases, UV–visible spectroscopy measurements were conducted on the pristine, MC, and MC&PI perovskite layers upon their thermal annealing (**Figure 2**). The changes in absorption peaks in low-n phases ($n = 2$, 3, or 4) and high-n phases demonstrate distinct trends as a function of thermal annealing time. Therefore, competition arises between the nucleation of low-n and high-n phases in quasi-2D perovskite during the annealing process.[26] An observation is evident in perovskite films in their pristine state: after 20 s of thermal annealing, the absorption intensity of high-n phases is significantly low, while the absorption peak corresponding to $n = 2$ is clearly prominent. This signifies the generation of a substantial quantity of low-n phase perovskites. As the annealing time progresses and the energy brings to the system increases, the absorption intensity from the high-n phases increases, while the low-n phase ($n = 2$) weakens. In the case of the MC sample (Figure 2b), after an 8 s annealing time, the absorption intensity of MC films in high-n phases is evident, while the absorption peaks corresponding to $n = 2$ remain distinct and strong. This indicates the generation of a significant number of low-n phase perovskites. With increasing annealing time, the absorption intensities from high-n phases become more pronounced, the low-n ($n = 2$) phase decreases in intensity while the low-n ($n = 3$) phase absorption peak increases. After 2 min of annealing time, the $n = 3$ absorption peak reduces in turn, implying a transformation from low-n phase into high-n phases.

In the case of MC&PI perovskite layers (Figure 2c), the nucleation process of high-n phases is nearly complete after a 5 s annealing time at 150 °C, as the absorption intensity attributed to high-n phase perovskites remains unchanged with increasing annealing time. As with the MC sample, an increase in n-phase is observed upon annealing. Therefore, MC&PI facilitates the homogeneity of the solution and promotes high-n phase seed formation, thereby suppressing the generation of low-n phases resulting from the aggregation of spacer cations and FA^+.[21] Consequently, this process leads to the dispersion of perovskite phases, where high-n phases are homogeneously distributed throughout the film.[24]

In order to gain further insights into the distribution of phases and the dynamics of charge in quasi-2D perovskite layers, steady-state photoluminescence (PL) spectra were measured. Figure S5 (Supporting Information) displays the steady-state PL spectra of perovskite layers with $n = 1/2/3$ compositions. The PL on the back of the layer was examined using an excitation wavelength of 470 nm. As illustrated in Figure 2e, the dominant PL peak for the MC&PI layer appears at 805 nm, which corresponds to the high-n phases. A weak emission peak at 576 nm ($n = 2$) is also detected. In contrast, besides the main peak, distinct emission peaks at ≈576, 640, and 682 nm are observed in the pristine layer, indicating the presence of low-n phases ($n = 2,3,4$) in the pristine quasi-2D perovskite layer. This finding is consistent with the UV–vis absorption data discussed earlier. Additionally, both the MC&PI and MC layers exhibit a stronger PL intensity compared to the pristine layer, indicating a reduced presence of traps and higher crystal quality in the perovskite layer, which results in decreased non-radiative recombination.[18] In general, quasi-2D perovskite precursor solutions typically include colloidal particles exhibiting an unpredictable size distribution. These particles have the potential to serve as sites for nucleation, leading to unfavorable crystal morphology in quasi-2D perovskite structures.[27] It is evident that MC&PI interacts with spacer cations and FA^+ within the quasi-2D perovskite system, resulting in the formation of a plentiful and uniform colloidal dispersion in the precursor solution. This interaction plays a crucial role in promoting the generation of a uniform composition during the crystallization process of quasi-2D perovskites.

Furthermore, we conducted a comparison of the photoluminescence (PL) spectra obtained from back (substrate) side and

© 2023 The Authors. Advanced Materials Interfaces published by Wiley-VCH GmbH

21967350, 2024, 6, Downloaded from https://onlinelibrary.wiley.com/doi/10.1002/admi.202300773 by HONG KONG POLYTECHNIC UNIVERSITY HUNG HOM, Wiley Online Library on [26/11/2024]. See the Terms and Conditions (https://onlinelibrary.wiley.com/terms-and-conditions) on Wiley Online Library for rules of use; OA articles are governed by the applicable Creative Commons License

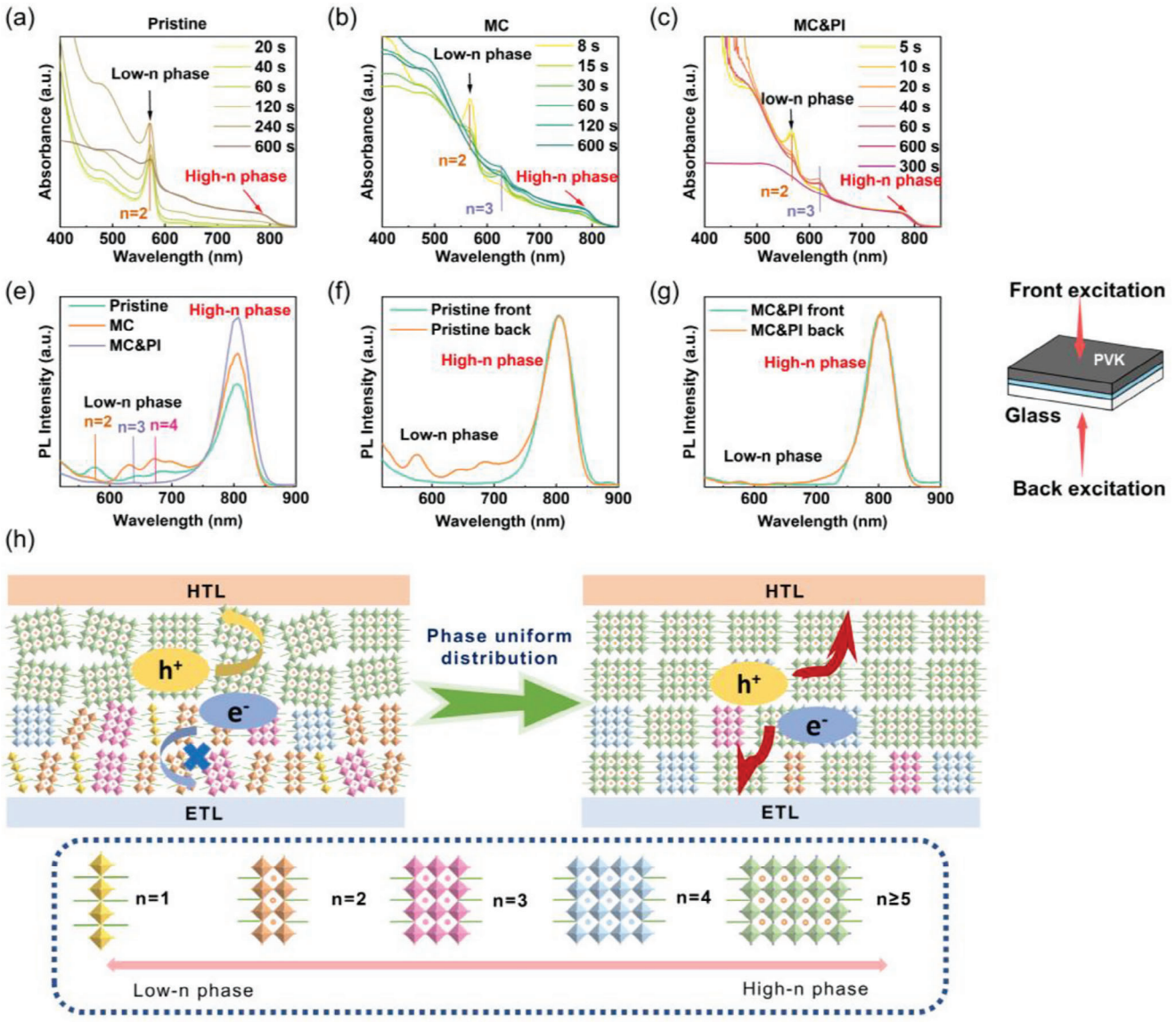

Figure 2. UV–vis absorption spectra evolution upon annealing at 150 °C: a) pristine, (b) MC, and (c) MC&PI perovskite layers. e) Photoluminescence (PL) spectra of pristine, MC, and MC&PI layers (back side). PL spectra were recorded from the back and front sides for f) pristine layers and g) MC&PI layers. h) Schematic description of the uniformization of phase distribution and conductive pathway.

front (air) side excitations (Figure 2f,g; Figure S6, Supporting Information). Under the back-side excitation configuration, significant PL emission was observed from the low-n phases in the pristine layer (predominantly $n = 2$) and the MC layer (predominantly $n = 3$ and $n = 4$). Conversely, under the front-side excitation configuration, the PL emission corresponded to the high-n phases in the pristine and MC layers. This indicates a nonuniform vertical distribution of the phases with the low-n ones being localized near the substrate and the high-n phase being found on the layer top. Typically, quasi-2D perovskite layers deposited through a solution-based approach consist of multiple 2D perovskite phases with varying n-values. These 2D perovskite phases with different n-values are randomly arranged, resulting in the formation of quantum wells with various widths, which consequently leads to significant energy disorder (Figure 2h).[22a] In the meantime, the charge mobility within the quasi-2D perovskite was impeded due to the dielectric mismatch caused by the substantial organic cations present in the low-n phases, thereby significantly impacting the photovoltaic performance of perovskite solar cells.[28] Under both the back and front side excitation configurations of MC&PI, more intense photoluminescence (PL) emission was observed solely from the high-n phases, suggesting a uniform vertical distribution of phases (Figure 2h).[29]

2.3. Solvent Elimination upon Thermal Annealing and Film Growth Types

To confirm that the inclusion of MC&PI additive promotes a significantly homogeneous distribution in FA-based quasi-2D

© 2023 The Authors. Advanced Materials Interfaces published by Wiley-VCH GmbH

21967350, 2024, 6, Downloaded from https://onlinelibrary.wiley.com/doi/10.1002/admi.202300773 by HONG KONG POLYTECHNIC UNIVERSITY HUNG HOM, Wiley Online Library on [26/11/2024]. See the Terms and Conditions (https://onlinelibrary.wiley.com/terms-and-conditions) on Wiley Online Library for rules of use; OA articles are governed by the applicable Creative Commons License

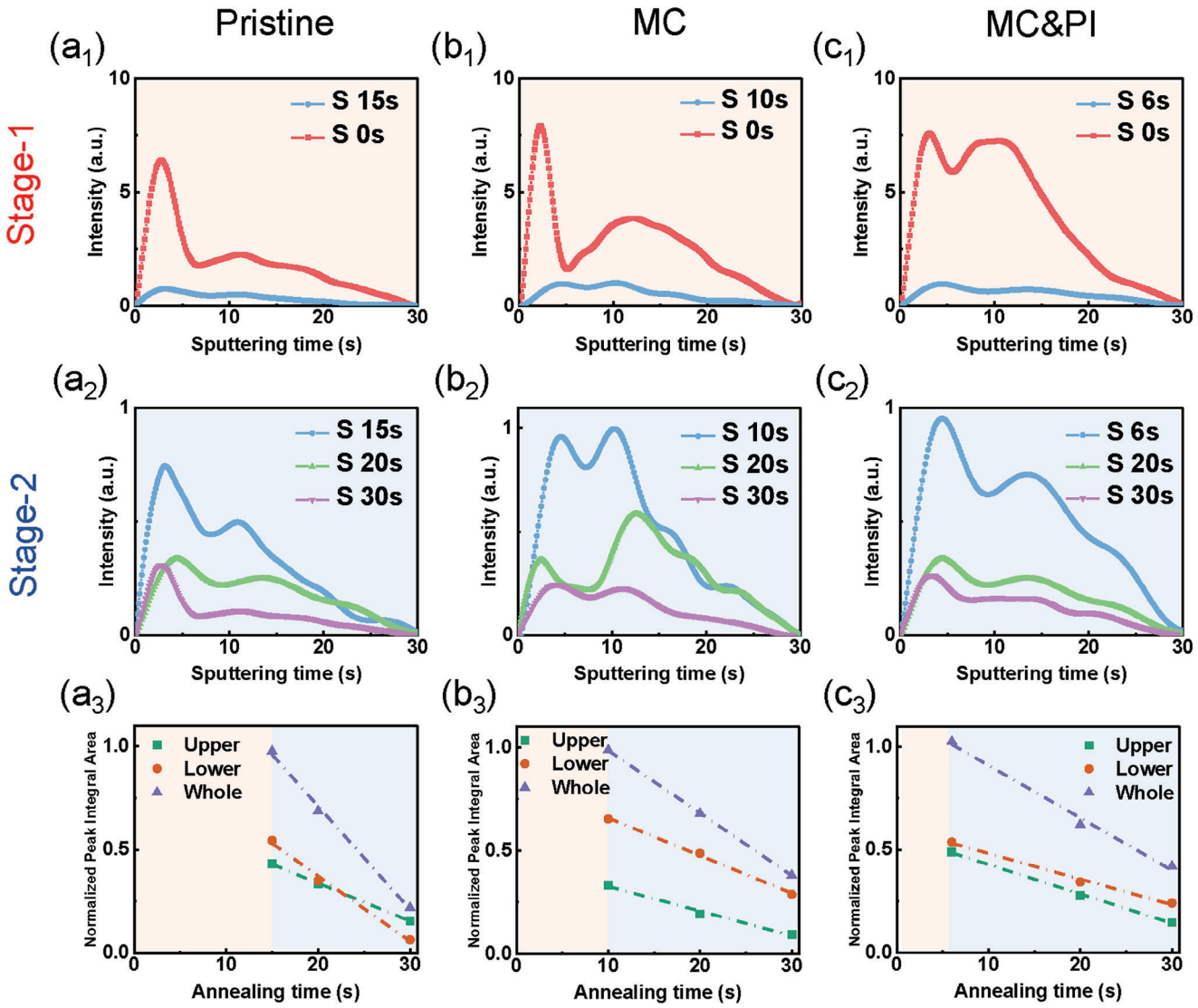

Figure 3. Evolution of GD-OES sulfur element (S) profile upon thermal annealing. Perovskite precursor films are followed upon Stage-1 and Stage-2 of thermal annealing. a_1) a pristine, (b_1) MC and (c_1) MC&PI films at stage-1. a_2) Pristine, (b_2) MC and (c_2) MC&PI films at Stage-2. Normalized peak integral area of the GD-OES S profiles for the upper layer, lower layer, and whole film at different annealing times: (a_3) pristine, (b_3) MC and (c_3) MC&PI. (Green dashed line: linear fit line of the upper layer in Stage-2; Red dashed line: linear fit line of the lower layer in Stage-2; Blue dashed line: whole film in Stage-2).

perovskite samples, we conducted a comprehensive investigation of the layer formation process during the thermal annealing using glow discharge optical emission spectroscopy (GD-OES) measurements. The principle of the technique is explained in Figure S7 (Supporting Information) and in the accompanying text. The advantages of the technique include its swiftness and the possibility of following the crystallization, stating from a precursor film soaked with structural solvent. Moreover, we have recently published a review paper on its working principle and reviewed the information that it can provide in the perovskite solar cell research field.[30] The interest of GD-OES here is the timeliness of the measurement, and the use of a soft vacuum to avoid a profound change in solvent content and distribution between the layer preparation and the end of the analysis. The removal of residual solvents is a critical step in the synthesis that occurs during the recrystallization and growth of the quasi-2D perovskite layer. This work is the first to describe the distribution of solvent molecules evolution upon the thermal annealing. It provides notably important information on the recrystallization and on the growth direction. The results on quasi-2D perovskite layers are analyzed based on our previous investigation of the formation of 3D perovskite films.[22,30] In our experiments, the solvent employed is a N,N-dimethylformamide (DMF)-dimethyl sulfoxide (DMSO) mixture, and the presence of the S element in DMSO enables its tracking through GD-OES. The S element profiles for various quasi-2D perovskite layers and increasing annealing times are presented in **Figure** 3a,b. In GD-OES, as the GD plasma sputtering time increases, deeper regions of the quasi-2D perovskite film are analyzed until reaching the meso-TiO_2 film. Figure S7 (Supporting Information) shows that the the

© 2023 The Authors. Advanced Materials Interfaces published by Wiley-VCH GmbH

21967350, 2024, 6, Downloaded from https://onlinelibrary.wiley.com/doi/10.1002/admi.202300773 by HONG KONG POLYTECHNIC UNIVERSITY HUNG HOM, Wiley Online Library on [26/11/2024]. See the Terms and Conditions (https://onlinelibrary.wiley.com/terms-and-conditions) on Wiley Online Library for rules of use; OA articles are governed by the applicable Creative Commons License

meso-TiO_2 layer is reached after a 25 s long sputtering time. Prior to annealing, the profile of DMSO exhibits a strong peak in the upper part of the spin-coated layer for pristine and MC samples (Figure 3a_1,b_1). On the other hand, the solvent distribution is remarkably homogeneous for MC&PI sample (Figure 3c_1).

Regarding the thermal annealing process, we have identified two distinct stages based on the film aspect (Figure S8, Supporting Information) and their XRD (Figure S9, Supporting Information). The initial layer composition varies with the initial solution composition. As found for the 3D perovskite, in the presence of MACl, the perovskite phase is detected and is pure for MC&PI. Upon Stage-1, the solvent is quickly removed. GD-OES shows that the near-surface sulfur peak disappears for the pristine and MC samples. Upon Stage-1, the active quasi-2D perovskite phase is formed through the decomposition of the precursor phase.[31]

During Stage-2, the quasi-2D perovskite phase grains undergo preferential growth in a specific direction, while the residual solvent continues to be eliminated. The initial composition of the intermediate plays a crucial role in regulating the speed and direction of grain growth, which is observed through the progressive elimination of solvent across the film thickness. GD-OES (Figure 3) shows that, in the pristine and MC samples, DMSO is slowly eliminated near the surface, while less solvent remains in the deeper region of the film. Based on our previous work on 3D perovskite growth mechanism,[22] the pristine quasi-2D perovskite layer has a profile typical of an upward growth of grains from the bottom to the top (Figure 3a_2). This promotes the formation of multiple and oblique grain boundaries, as well as relatively small quasi-2D perovskite grains. In the presence of MC in perovskite precursor solution(Figure 3b_2), the S profiles exhibit differences compared to the pristine sample. The second peak decreases at a slower rate than the primary peak, and the gap between them is not as pronounced as in the pristine sample. This results in the formation of a denser quasi-2D perovskite layer. With the inclusion of MC&PI, the S profiles exhibit distinct characteristics (Figure 3c_2). The S profile is distributed more evenly throughout the film thickness. Upon annealing, the solvent profile decreases uniformly across the entire film thickness. This suggests that a lateral grain growth occurs, leading to the formation of uniform quasi-2D perovskite layers with large monolithic grains, as demonstrated in the cross-section SEM image (Figure 1b).

To rationalize the analysis, we divided the film into upper and lower parts and we employed the approach and quantitative tools developed for 3D perovskite in Ref. [22] and described in Figure S10 (Supporting Information). In Figure 3(a_3–c_3), we present the integrals for each film at various annealing times. We determined that the (re)crystallization took place during Stage-1, while the layer growth predominantly occurred in Stage-2. In Stage-2, we observed solvent removal at a relatively constant rate, and we calculated the slopes of two linear fits: SUS-2 slope for the upper layer and SLS-2 slope for the lower layer. Subsequently, we established a parameter indice that relates to the relative growth speed of each layer parts.[22] The index, short-named GI, stands for Gap Index and is defined as:

$$GI(\%) = (SUS-2 - SLS-2) * 100/Max\{SUS-2, SLS-2\} \quad (1)$$

The values of SUS-2 and SLS-2 are provided in **Table 1**. By analyzing and comparing the slopes of the two curves (Table 1), we can accurately determine the direction of layer growth for different perovskites. GI serves as the primary parameter for quantifying the differences in layer growth among perovskites (Table 1).

Table 1. Effect of additives on the solvent elimination speed: Slopes, GI(%) parameter, and global growth direction.

System	Additive	SUS-2[a)]	SLS-2[b)]	GI[c)] [%]	Global growth direction
(PMA)2$FA_4Pb_5I_{16}$	Pristine	−0.01835	−0.03158	−41.9	Upward
	MC	-0.01193	-0.01825	-34.6	Upward
	MC&PI	-0.01427	-0.01145	+19.7	Lateral

They are extracted from the linear fit lines of upper layer and lower layers at stage-2 (Figure 3); [a)] SUS-2 : The Slope of Upper layer in the Stage-2; [b)] SLS-2 : The Slope of Lower layer in the Stage-2; [c)] GI (Gap Index) = (SUS-2 – SLS-2) × 100/Max{SUS-2,SLS-2}.

From **Figure 4** and Table 1, we can draw the following conclusions: i) When SLS-2 is lower than SUS-2 with GI lower than −30%, the quasi-2D perovskite layer grows upward, from bottom to top. This applies to the pristine and MC samples. In such cases, multiple and oblique grain boundaries are formed, resulting in relatively small perovskite grains. Additionally, these layers exhibit higher roughness compared to films produced through lateral growth. The growth mode of these two layers is defined as Type II. ii) In contrast, when the slope of the upper film of MC&PI in stage-2 (SUS-2) is very close to that of the lower film in stage-2 (SLS-2), it leads to the formation of uniform layers with large monolithic grains. We refer to this growth trend as lateral growth. This phenomenon is observed in the MC&PI samples, which exhibit a monolithic architecture in Figure 1b. The latter, is defined as Type III growth mode in our Ref. [22] It produces a monolithic structure with reduced and vertically oriented grain boundaries, resulting in smoother films. It facilitates fast charge transport to the contact at both sides of the MHP layer in the solar cells.

One remarkable finding of this study is that the co-additives, MC&PI, regulate the solvent elimination and consequently control the growth of the quasi-2D perovskite layer throughout its entire depth. They enhance the quality of the layer, as evidenced by significant improvements in crystalline quality. Importantly, our findings demonstrate that the location and density of the initial seeds/crystallites, determined by the microstructure and composition of the precursor film, dictate subsequent steps, particularly the direction of film growth, as shown in the middle part of Figure 4. Their density influences the final size of crystals in the quasi-2D perovskite film. The MC&PI additives control the layer formation from the early stages and play a crucial role in modulating the size and composition of precursor aggregates and initial nuclei.

MC&PI enhances the dispersion of PMA^+ spacer cations and FA^+ during the recrystallization process. Sparsely dispersed crystallites are desired as they facilitate the growth of large grains that contribute to the final performance of the devices. In general, additives improve the homogeneity of nucleation sites, promote larger precursor crystallites, regulate the solubility of precursor solutes and the composition of crystallized intermediate phases, and influence the speed of solvent removal and film growth.

© 2023 The Authors. Advanced Materials Interfaces published by Wiley-VCH GmbH

21967350, 2024, 6, Downloaded from https://onlinelibrary.wiley.com/doi/10.1002/admi.202300773 by HONG KONG POLYTECHNIC UNIVERSITY HUNG HOM, Wiley Online Library on [26/11/2024]. See the Terms and Conditions (https://onlinelibrary.wiley.com/terms-and-conditions) on Wiley Online Library for rules of use; OA articles are governed by the applicable Creative Commons License

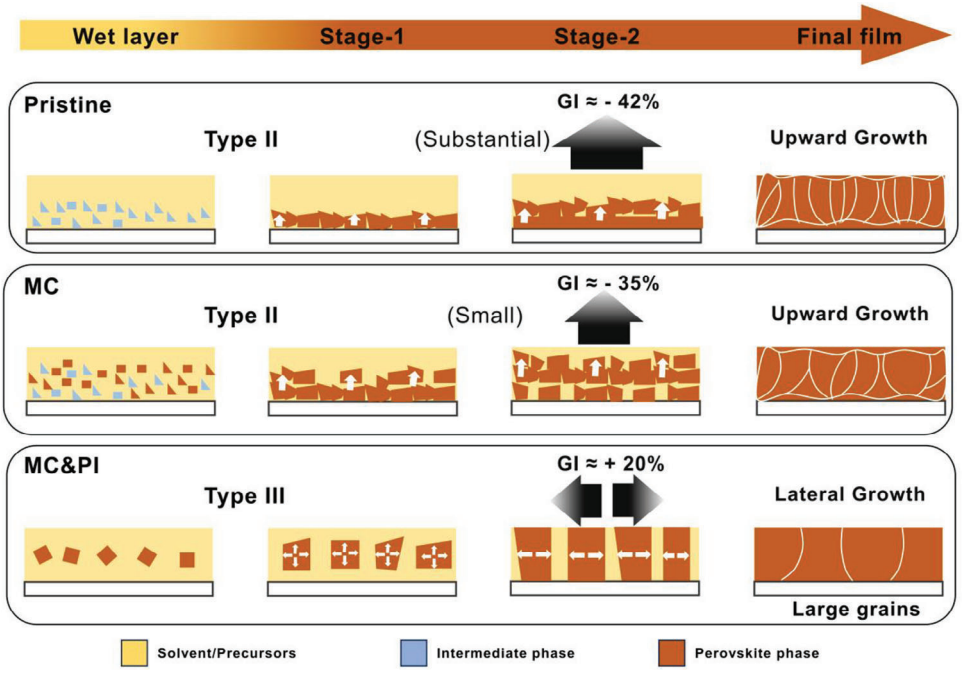

Figure 4. Schematic of perovskite layer formation during thermal annealing. Classification of perovskite layer growth: Direction and mechanism of grain growth, along with growth parameters. The white arrows indicate the directions of growth.

By combining the information presented in Figures 2 and 3, we can draw the following conclusion:

- For the pristine sample, an initial low-n phase ($n = 2$) predominantly forms on the layer bottom, Followed by the gradual upward growth of the high-n phase.
- For the MC sample, the initial low-n phase ($n = 2$) and a certain proportion of the high-n phase are primarily generated on the lower layer part, with subsequent upward growth, accompanied by the conversion of the low-n phase ($n = 2$) into a less pronounced low-n phase ($n = 3$).
- For the MC&PI sample, the low-n phase ($n = 2$) and high-n phase initially develop uniformly in the lateral direction, followed by the gradual conversion of $n = 2$ into $n = 3$ as an intermediate phase. Then most low-n phase components transform into higher n phase in the same lateral direction.

The explanation lies in the fact that the gradual crystallization process (indicated by GD-OES slope), facilitated by MC&PI, results in the reorganization of organic spacer cations and FA^+ within the quasi-2D perovskite structure. This, in turn, strongly reduces the formation of low-n phases that are typically induced by the aggregation of spacer cations. Due to the reorganization of spacer cations and FA^+, the low-n phases tend to undergo a transformation into high-n phases. By incorporating MC&PI, the occurrence of low-n phases is greatly minimized, with a corresponding increase in high-n phases, indicating the effective conversion from low-n to high-n phases. It results in exceptional pathways for efficient carrier extraction, leading to enhanced charge transport within the quasi-2D perovskite layer (Figure 2h). For MC&PI film, the high-n phase of the whole perovskite film is very homogeneous with perovskite slabs largely oriented perpendicular to the substrate, which is favorable to the charge transfer process. In the pristine film, the distribution of different *n*-value perovskite phases is not uniform throughout the perovskite film, and the low-n-value perovskite phase is mainly found at the bottom part of the perovskite film. Moreover, the orientation of high-n phase is more random than that of MC&PI film, which is unfavorable to the charge transfer process.

2.4. Photovoltaic Capability of the Perovskite Solar Cells

Subsequently, we fabricated n–i–p heterojunction perovskite solar cells using the pristine, MC, and MC&PI perovskite layers, employing a glass/FTO/TiO_2/perovskite/spiro-OMeTAD/Au architecture (Figure S11, Supporting Information). The *J*–*V* characteristics under standard AM 1.5G illumination are presented in **Figure 5b**.

The optimized concentration of MACl was determined as 40% (molar ratio of FAI), to get pinhole-free films and the best crystallinity (Figure S2, Supporting Information), consistent with that of device performance (Table S1, Supporting Information). The optimized PbI_2 excess was also determined as 20% (molar ratio of PbI_2 compared to stoichiometric PbI_2) based on the device performance (Tables S2 and S3, Supporting Information).

The pristine-based device ($n = 5$) exhibited a *PCE* of only 2.61%, a J_{SC} of 6.76 mA cm^{-2}, a V_{OC} of 1.003 V, and an *FF* of 38.52% (**Table 2**). These samples gather many deleterious properties. The pristine sample contains pinholes and is made of coarse grains (Figure 1b and Figure S1, Supporting Information). On the cross-sectional view, voids can be observed between the TiO_2 layer and the perovskite layer (Figure 1b) XRD, absorbance and PL measurements show that the pristine perovskite is made of

© 2023 The Authors. Advanced Materials Interfaces published by Wiley-VCH GmbH

21967350, 2024, 6, Downloaded from https://onlinelibrary.wiley.com/doi/10.1002/admi.202300773 by HONG KONG POLYTECHNIC UNIVERSITY HUNG HOM, Wiley Online Library on [26/11/2024]. See the Terms and Conditions (https://onlinelibrary.wiley.com/terms-and-conditions) on Wiley Online Library for rules of use; OA articles are governed by the applicable Creative Commons License

21967350, 2024, 6, Downloaded from https://onlinelibrary.wiley.com/doi/10.1002/admi.202300773 by HONG KONG POLYTECHNIC UNIVERSITY HUNG HOM, Wiley Online Library on [26/11/2024]. See the Terms and Conditions (https://onlinelibrary.wiley.com/terms-and-conditions) on Wiley Online Library for rules of use; OA articles are governed by the applicable Creative Commons License

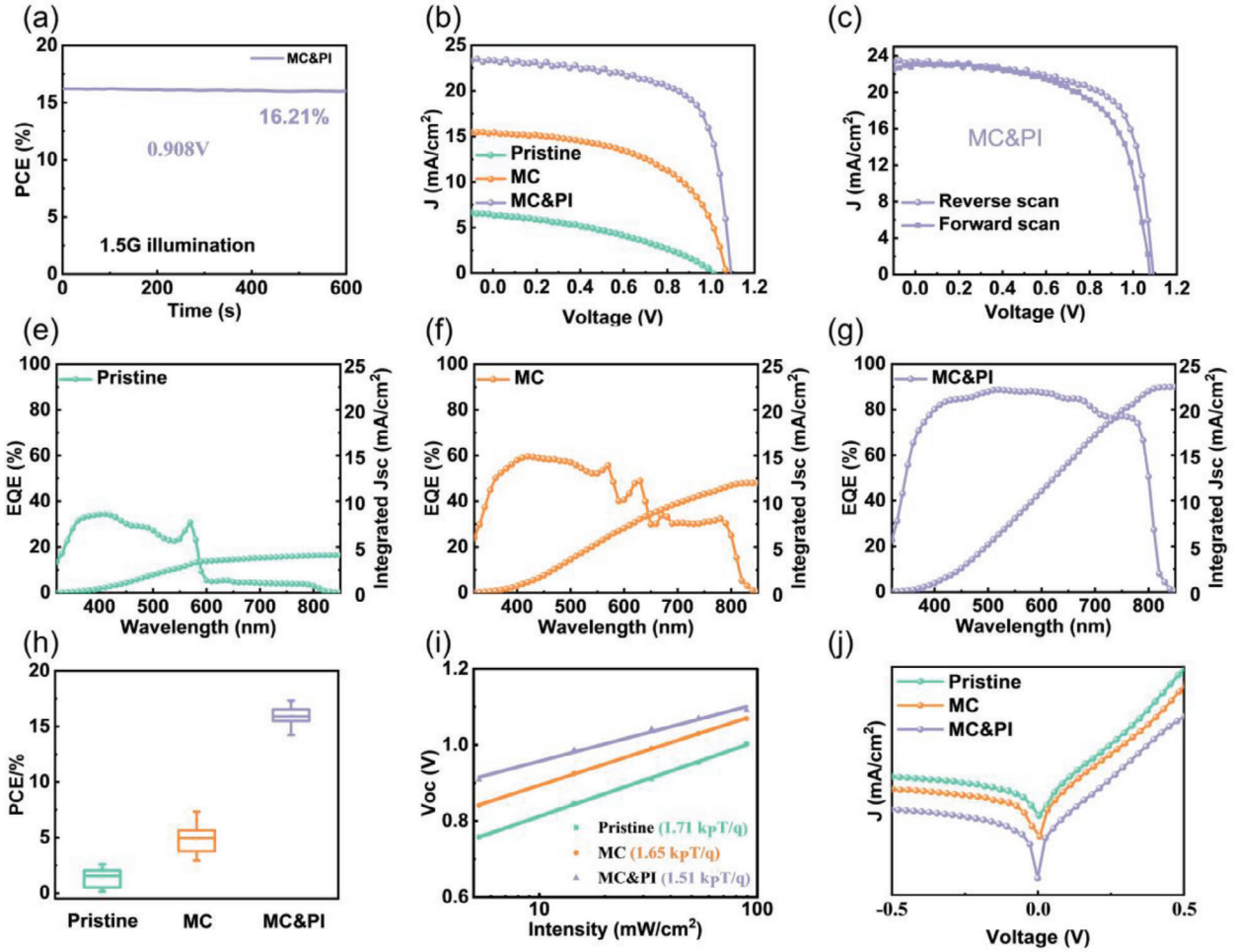

Figure 5. a) Normalized *PCE* of maximum power point tracking curve of MC&PI cell in air at 25 °C with 50–55% RH. b) Reverse scan *J–V* characteristics of the pristine, MC, and MC&PI perovskite solar cells. c) Forward and reverse scans for the MC&PI solar cell. e,g) External quantum efficiency (EQE) and integrated short-circuit current (J_{sc}) of the leading cells for the pristine, MC, and MC&PI perovskite solar cells. h) Histogram illustrating the distribution of efficiencies for the pristine, MC, and MC&PI perovskite solar cells. i) Dependence of open-circuit voltage (V_{OC}) on light power density. j) Dark *J–V* curves of the pristine, MC, and MC&PI perovskite solar cells.

a mixture of quasi-2D phases with different low-n values. Especially, the $n = 2$ perovskite is present, notably at the film bottom, and this phase delivers low performances. The bottom low-n has a larger bandgap. Moreover, *n* decrease creates an energy band upward shift.[32–35] Both lead to an energy barrier with the TiO_2 electron transporting layer that strongly reduces the charge transfer. Furthermore, the 2D phase is oriented with the inorganic slabs parallel to the surface. This orientation is detrimental for the charge transfer as it creates energy barriers for the charge transfer across the perovskite slabs. The low absorbance of the pristine film is also detrimental for the performance (Figure 1e).

Table 2. Photovoltaic *J–V* parameters, *PCE*, and *HI* of the best cells.

Cell $n = 5$	Scan direction	V_{OC} /V	Jsc [mA cm^{-2}]	*FF* /%	*PCE* /%	*HI*[a] /%
Pristine	Reverse	1.003	6.76	38.52	2.61	33
	Forward	0.989	4.78	36.67	1.73	
MC	Reverse	1.069	12.50	54.85	7.33	27
	Forward	1.040	10.65	48.52	5.37	
MC&PI	Reverse	1.098	23.43	68.87	17.71	12
	Forward	1.073	22.83	63.17	15.47	

[a] Hysteresis index : $HI(\%) = (PCE_{rev} - PCE_{for}) \times 100/PCE_{rev}$

The MACl-based ($n = 5$) device showed a significantly improved PCE of 7.33% with a V_{OC} of 1.069 V, J_{SC} of 12.50 mA cm^{-2}, and *FF* of 54.85%. Encouragingly, the MC&PI PSC achieved a champion PCE of 17.71% with a V_{OC} of 1.098 V, J_{SC} of 23.43 mA cm^{-2}, and *FF* of 68.87%. Remarkably, the PCE of this study is near the highest reported PCE for PMA-based $n < 6$ 2D halide perovskite devices, demonstrating its competitiveness (Table S4, Supporting Information).[36] MC&PI-based devices exhibited higher V_{OC} and J_{SC} compared to pristine devices. Noteworthily, the adding of PbI_2 and MACl changes the chemical formula of the perovskite. Getting the final composition of the perovskite film after addition is difficult. If we consider that the formed quasi-2D perovskite is an iodide, we obtain a general

© 2023 The Authors. Advanced Materials Interfaces published by Wiley-VCH GmbH

formula of $PMA_2FA_4MA_{0.66}Pb_{5.66}I_{18}$, so the new $n = 5.66$. If chloride is incorporated, we can then write a new general formula: $PMA_2FA_4MAPb_6I_{18}Cl$ and $n = 6$. The conclusion is that the dramatic increase in PCE is not attributable to the n increase which is small.

To further demonstrate the photoelectric performance of MC&PI PSC, we conducted a steady-state photocurrent measurement and analyzed the steady PCE output under standard AM 1.5G illumination for 300 s while maintaining the voltage at the maximum power points (Figure 5a). The MC&PI devices exhibited a steady *PCE* of 16.21%, indicating excellent operational stability in the illuminated environment. The addition of MC&PI substantially improved the crystal quality and facilitated the low dispersion in n phase. It enabled the efficient charge transport through the widespread (111) oriented high-n phase, the good charge transfer to TiO_2, and it resulted in a significantly enhanced and stable J_{SC} in the MC&PI PSC.

To compare the occurrence of hysteresis in MC&PI perovskite solar cells, we conducted forward and reverse scans of the devices, as shown in Figure 5c. The MC&PI PSCs exhibited minimal hysteresis index (HI). Additionally, we statistically analyzed the distribution of PCE for the pristine, MC, and MC&PI devices (Figure 5h), revealing a higher average PCE and improved reproducibility. Figure S12 (Supporting Information) displays the distribution of J_{SC}, V_{OC}, *FF*, and HI for the pristine, MC, and MC&PI devices. Notably, the MC&PI devices demonstrated a narrow distribution in V_{OC} and *FF*, indicating high reproducibility.

Figure 5e,g presents the external quantum efficiency (EQE) and integrated J_{SC} of the pristine, MC, and MC&PI quasi-2D perovskite solar cells. Particularly, the MC&PI device exhibited an integrated J_{SC} of 22.48 mA cm^{-2}, which closely matched the measured value from the *J–V* curve. In contrast, the pristine devices showed an integrated J_{SC} of 4.09 mA cm^{-2}, indicating superior charge transport and reduced carrier recombination of MC&PI, validating the effectiveness of MC&PI in improving the growth of high-n phases.

By analyzing the relationship between V_{OC} and the logarithm of the incident light power density, we determined the ideality factor n through the slope nkT/q (Figure 5i). The MC&PI device exhibited the smallest n at 1.51, confirming the reduction of trap-assisted recombination. This can be attributed to MC&PI's ability to narrow phase distribution and to govern the growing direction, reducing inner traps caused by perovskite during the crystallization process and minimizing inner bulk traps, thereby lowering trap-assisted recombination.[9a]

To further investigate the charge recombination of various devices, dark *J–V* curve measurements were performed, as shown in Figure 5j. It can be observed that the dark current density of the MC&PI device is diminished compared to MC and pristine. It is in agreement with the higher *V*oc and confirms a lower presence of bulk traps in the quasi-2D PSC.

2.5. Stability Study of Perovskite Layers and Devices

The stability of layers against moisture is a crucial factor in the commercialization of perovskite solar cells, thus the stability tests of pristine, MC, and MC&PI layers under the corresponding conditions are presented. MC&PI presented reduced grain boundary formation, thereby reduced water permeation and a significantly improved humidity stability. Photographic images of the pristine, MC, and MC&PI layers were captured under continuous aging conditions of 25–55% RH at 25 °C in ambient air (Figure S13, Supporting Information), further confirming the enhanced humidity stability of MC and MC&PI layers.

Figure 6a–c displays the XRD patterns of the aged layers at 25 °C with 25–55% RH in ambient air. The pristine layer degraded rather quickly. The α-phase peak intensity was strongly decreased and gave way to a strong δ-phase peak after 720 h of aging. This instability is due to the absence of small cation (MA^+) in the lattice which is required for the α-phase stabilization. On the other hand, even after 720 h, the aged MC&PI perovskite layers only showed a weak peak of lead iodide and a slight decrease in the intensity of the perovskite peaks, indicating that the MACl and PbI_2 excess addition significantly enhanced the environmental stability of the quasi-2D perovskite layer in ambient air. The improved thermal and humidity stability of the layers are attributed to both the hydrophobicity of large PMA^+ cation and the MC&PI process, which substantially reduce the formation of grain boundaries, defects, and limits moisture intrusion.

We calculated the relative peak intensity of the high-n phases for the pristine, MC, and MC&PI during aging (Figure S14, Supporting Information). The MC&PI layers exhibited excellent phase stability, contributing to the improved structural stability of the $PMA_2FA_{n-1}Pb_nI_{3n+1}$ phases.

Based on the aforementioned stability test of the quasi-2D perovskite layer, tests of the corresponding devices under various conditions were further evaluated. In a N_2 glovebox, the efficiencies of the MC&PI solar cells remained at approximately 100% for 2 months (Figure 6d). Figure 6e shows the normalized *PCE* variation curves of unsealed pristine, MC, and MC&PI devices that underwent aging in ambient air at 25 °C with 25–55% RH. The pristine device exhibited the poorest stability during the humidity aging process, with a clear decrease in *PCE* after 480 h. In contrast, the MC&PI device demonstrated the highest stability, with over 89% of the initial *PCE* retained. Under continuous light exposure, the efficiency was maintained at the same level for 5 h (Figure 6f). This is because MC&PI drastically reduces the formation of grain boundaries, thereby limiting water intrusion and significantly improving the humidity stability of perovskite solar cells.

3. Conclusion

In conclusion, MACl and PbI_2 were employed as perovskite precursor solution additives to homogenize the formed phases and enhance the quality of FA-based 2D perovskite layers. Our extended investigation of the film formation process has shown that MACl expedited the confine crystallization and phase reorganization in the quasi-2D FA-based perovskite, facilitating the transition from the low-n phase to the (111) oriented high-n phase in the FA-based quasi-2D perovskite. Simultaneously, adding an excess of PbI_2 significantly inhibited the aggregation of colloids in the precursor solution, thereby improving the crystallization of the high-n phase during the annealing process. The abundant high-n phase coexisting with the low-n phase was uniformly dispersed within the perovskite, creating a continuous pathway for charge transport throughout the layer. We systematically

© 2023 The Authors. Advanced Materials Interfaces published by Wiley-VCH GmbH

21967350, 2024, 6, Downloaded from https://onlinelibrary.wiley.com/doi/10.1002/admi.202300773 by HONG KONG POLYTECHNIC UNIVERSITY HUNG HOM, Wiley Online Library on [26/11/2024]. See the Terms and Conditions (https://onlinelibrary.wiley.com/terms-and-conditions) on Wiley Online Library for rules of use; OA articles are governed by the applicable Creative Commons License

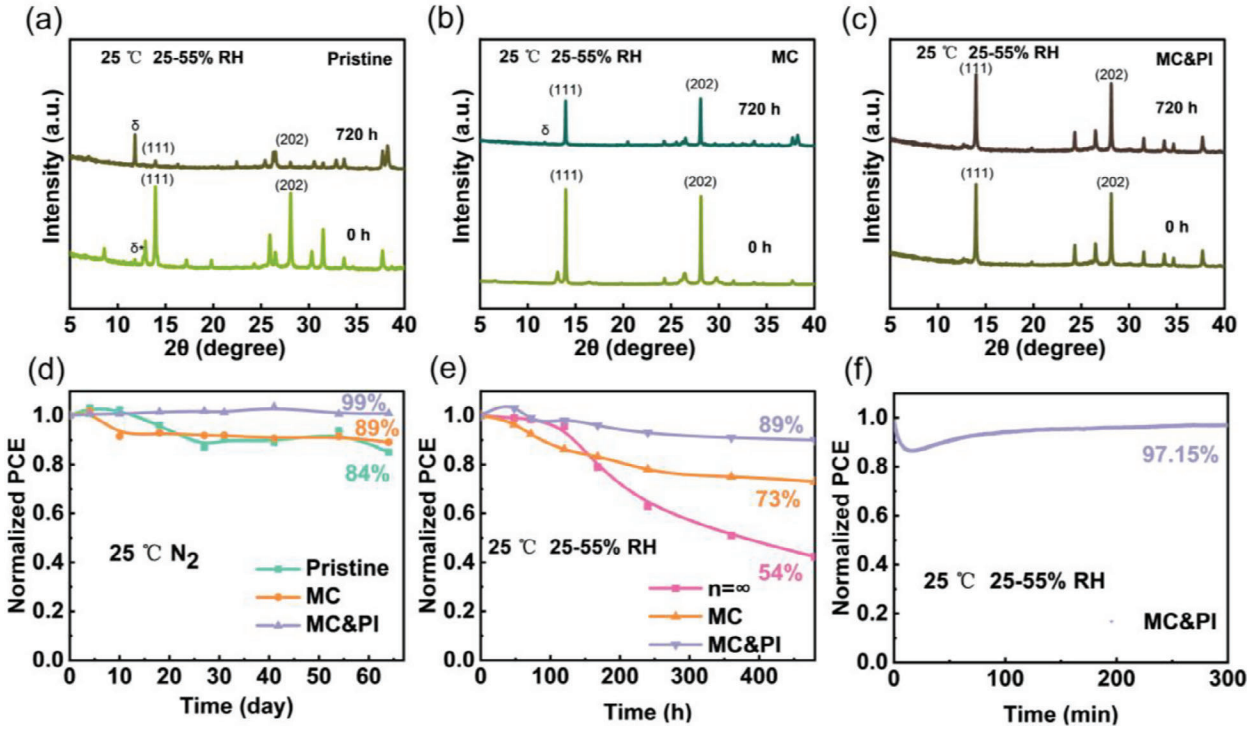

Figure 6. XRD patterns of a) pristine, b) MC, and c) MC&PI perovskite layers pre- and post-aged at 25 °C in the air with 25–55% RH. d) Normalized *PCE* variation curves of unsealed pristine, MC, and MC&PI devices at 25 °C store in N_2. e) Standardized *PCE* of unsealed 3D perovskite ($FA_{1-x}MA_xPbI_3$) ($n = \infty$), MC and MC&PI quasi-2D devices in the air at 25 °C with 25–55% RH for extended stability testing. f) Normalized *PCE* of maximum power point tracking curve of MC&PI cell in air at 25 °C with 25–55% RH for extended stability test.

investigated the impact of MC and MC&PI on solvent evaporation and layer growth direction in the layer formation process using the GD-OES technique. We show the altering of the growth direction of the FA-based perovskite layer from an upward growth (Type II) to a lateral growth (Type III). The electron trap densities in the MC and MC&PI devices were significantly reduced compared to the pristine sample, aligning with the longer carrier lifetime and diffusion length. Therefore, MC&PI effectively decreased trap states and suppressed non-radiative recombination in the devices, resulting in a reduction of trap density within the layer. It also suppresses the energy barrier with the bottom contact layer. The dual additive composition has been optimized. Finally, the efficiency of the FA-based quasi-2D device with MC&PI layer was enhanced to 17.71%, and the corresponding devices exhibited high stability.

4. Experimental Section

Materials: N,N-dimethylformamide (DMF, 99.8%), dimethyl sulfoxide (DMSO, 99.9%), isopropanol (IPA, 98%), 4-tert-butylpyridine (96%), acetonitrile (99.8%), chlorobenzene (CB, 99.8%) and lithium bis(trifluoromethanesulfonyl)imide (99.95%) were purchased from Sigma-Aldrich. Lead iodide (PbI_2, 99.9985%) was purchased from TCI Europe N.V.. TiO_2 NR30-D paste, formamidinium iodide (FAI, 99.99%) and Phenylmethylammonium iodide (phenylmethylamine hydroiodide or benzylammonium iodide, PMAI 99.5%) were obtained from Greatcell Solar Materials. 2,2′,7,7′-tetrakis-(N,N-di-p-methoxyphenylamine)−9,9′-spirobifluorene (spiroOMeTAD, ≥99.8%) was purchased from Borun New Materials Technology LTD.. All chemicals were used as received without further purification. Fluorine-doped SnO_2 (FTO) coated glass substrates is TEC 7 from Pilkington.

Preparation of Substrates, Compact TiO_2, and Mesoporous TiO_2 Layers: Fluorine-doped SnO_2 (FTO) substrates were etched through zinc powder and 10% HCl solution and then cleaned with soap and water. The substrates were subsequently immersed in a concentrated 2.2 M NaOH ethanol/water (10:1 v/v %) for 20 min and then cleaned with deionized water under ultrasonics for 15 min. The substrates were heated at 500 °C for 15 min. The TiO_2 compact film (noted c-TiO_2) was deposited by an aerosol spray pyrolysis process. The formed TiO_2 film was dense, pinhole-free and 30–35 nm thick. The TiO_2 nanoparticle solution for the preparation of the mesoporous film (noted mp-TiO_2) was prepared in advance and stirred for at least 12 h.[37] The TiO_2 NR30-D paste was diluted in ethanol with a 1:7 w/w ratio. The mesoporous film was spin-coated by dropping 45 µL of the TiO_2 solution on the compact TiO_2 film and then quickly transferred to a hotplate at 70 °C and dried for 5–10 min. Finally, the mp-TiO_2 was heated at 500 °C under an air flux for 30 min, cooled down to 200 °C, and removed from the hotplate. The thickness values of the mesoporous TiO_2 ranged between 120 nm and 150 nm.

Preparation of 2D Perovskite Layers: $(PMA)_2FA_4Pb_5I_{16}$ perovskite precursor solutions were prepared by dissolving specific stoichiometric quantities of PMAI (61.11 mg), FAI (89.42 mg) and PbI_2 (299.65 mg) in DMSO/DMF (100 µL: 400 µL volume ratio) mixed solution. The PbI_2 concentration was 1.3 M. MACl additive with a concentrations of 40 mol% of FAI was added into the precursor solutions. PbI_2 excess with concentrations of 20 mol% of stoichiometric PbI_2 was added into the precursor solutions. The solutions were primary stirred for a minimum of 2 h at room temperature in a N_2 glovebox. Forty five microliters of this solution was placed on top of the substrates. A two-step spin-coating program was introduced: primary spinning at 1000 rpm for 10 s and then at 6000 rpm for 30 s. Chlorobenzene (100 µL) was dripped 20 s after the

© 2023 The Authors. Advanced Materials Interfaces published by Wiley-VCH GmbH

21967350, 2024, 6, Downloaded from https://onlinelibrary.wiley.com/doi/10.1002/admi.202300773 by HONG KONG POLYTECHNIC UNIVERSITY HUNG HOM, Wiley Online Library on [26/11/2024]. See the Terms and Conditions (https://onlinelibrary.wiley.com/terms-and-conditions) on Wiley Online Library for rules of use; OA articles are governed by the applicable Creative Commons License

starting of the spinning routine. The layers were then annealed at 153 °C for 15 min.

Device Manufacture: A fresh solution was manufactured by dissolving 78 mg of spiro-OMeTAD in 1 mL of chlorobenzene. The Cobalt (Co) doped spiro-OMeTAD layer was manufactured through doping 18 µL tris(2-1H-pyrazol-1-yl)−4-tert-butylpyridine)-cobalt(III) tris (bis(trifluoromethylsulfonyl)imide) (376 mg in 1 mL acetonitrile) in the spiro-OMeTAD precursor solution. The lithium (Li) and Co doped spiro-OMeTAD layer was manufactured through doping 18 µL Co-salt solution, 23 µL bis(trifluoromethylsulfonyl)imide lithium salt solution (Li-TFSI) (517 mg in 1 mL ACN) and 39 µL TBP (tert-butylpyridine) in the spiro-OMeTAD precursor solution. The samples coated with spiro-OMeTAD layer were transferred into a nitrogen filled glovebox for one night. The devices were then completed by evaporating an 80 nm thick gold contact in a vacuum chamber.

Characterizations: The morphology of perovskite thin layers was measured in a field-emission SEM equipment (Zeiss Supra 40) in the in-lens mode. The structure of the organometal lead perovskite layers was characterized through a PANanalytical X-Pert high-resolution X-ray diffractometer (XRD) operated at 40 kV and 45 mA and applying the Cu Kα radiation with $\lambda = 1.5406$ Å. The layer specular absorbance was measured by a Cary 5000 UV–vis-NIR spectrophotometer. A glass/FTO/c-TiO_2/mp-TiO_2 sample was introduced for the baseline. The photoluminescence spectra were measured by a Cary Eclipse fluorescence spectrophotometer.

Glow-Discharge Optical Emission Spectrometry (GD-OES) analyses were performed by a HORIBA Jobin Yvon GD Profiler 2 equipment. This instrument was equipped with a RF-generator (at 13.56 MHz), a standard HORIBA Jobin Yvon glow discharge source with a cylindrical anode of 4 mm inner diameter and two optical spectrometers (a polychromator and a monochromator) for fast-optical detection. The Ar plasma was generated at an Ar pressure of 420 Pa and an applied power of 17 W. The precursor or perovskite film was mounted on an O-ring at one side of the plasma chamber and adopted as a cathode. The interests of the technique was its rapidity and easiness for use. It did not need high vacuum nor specific sample preparation (See Supporting Information). Therefore, the films could be characterized rapidly (less than 1 min) after each step of preparation.

GIWAXS measurements were performed using a microfocus X-ray source (IµS, Incoatec, Germany) producing Cu Kα radiation ($\lambda = 1.54$ Å). GIWAXS patterns were recorded with a 2D X-ray detector (Pilatus 100 K, Dectris, Switzerland) with an exposure time of 10 s. The incidence angle was set at 1° and the distance between the sample and the detector at 73 mm.

The *J–V* curves were recorded by a Keithley 2410 digital sourcemeter, applying a 0.1 V s^{-1} voltage scan rate. The solar cells were illuminated with a solar simulator (Abet Technology Sun 2000) filtered to mimic AM 1.5G conditions (100 mW cm^{-2}). The illuminated surface was delimited through a black mask with an aperture diameter of 3 mm. The power density was calibrated at 100 mW cm^{-2} using a reference silicon solar cell. The tracking experiments were performed under ambient conditions. The current was followed at the voltage of the maximum power. The external quantum efficiency (EQE) spectra were measured by an Oriel QUANTX-300 system.

Supporting Information

Supporting Information is available from the Wiley Online Library or from the author.

Acknowledgements

M.L. thanks the CSC for funding his Ph.D. scholarship (grant number 202 008 120 110). The ANR agency is acknowledged for financial support via the ChemSta project ANR-21-CE05-0022. The authors acknowledge the financial support of APVV-20-0111 and APVV-21-0297.

Conflict of Interest

The authors declare no conflict of interest.

Data Availability Statement

The data that support the findings of this study are available from the corresponding author upon reasonable request.

Keywords

additive compounds, crystallization mechanism, phase distribution, Rudlesden–Popper 2D perovskite, solar cells

Received: September 14, 2023
Revised: December 4, 2023
Published online: December 21, 2023

[1] a) H. Zhou, Q. Chen, G. Li, S. Luo, T.-B. Song, H.-S. Duan, Z. Hong, J. You, Y. Liu, Y. Yang, *Science* **2014**, *345*, 542; b) B. Saparov, D. B. Mitzi, *Chem. Rev.* **2016**, *116*, 4558; c) M. Ulfa, T. Zhu, F. Goubard, T. Pauporté, *J. Mater. Chem. A* **2018**, *6*, 13350; d) T. Zhu, D. Zheng, J. Liu, L. Coolen, T. Pauporté, *ACS Appl. Mater. Interfaces* **2020**, *12*, 37197; e) M. Li, H. Li, Q. Zhuang, D. He, B. Liu, C. Chen, B. Zhang, T. Pauporté, Z. Zang, J. Chen, T. Pauporté, *Angew. Chem., Int. Ed.* **2022**, *61*, e202206914; f) D. M. Zheng, T. Zhu, T. Pauporté, *Sol. RRL.* **2021**, *5*, 2100010.
[2] X. Meng, Z. Xing, X. Hu, Y. Chen, *Chinese J. Polym. Sci.* **2022**, *40*, 1522.
[3] a) J. Huang, Y. M. Li, H. Wang, F. H. Zhang, D. Zhang, *ACS Appl. Energy Mater.* **2022**, *14*, 20230; b) M. Shao, T. Bie, L. Yang, Y. Gao, X. Jin, F. He, N. Zheng, Y. Yu, X. Zhang, *Adv. Mater.* **2022**, *34*, 2107211.
[4] J. Zhao, Z. Zhang, G. Li, M. H. Aldamasy, M. Li, A. Abate, *Adv. Energy Mater.* **2023**, *13*, 2204233.
[5] J. Wu, H. Zeng, Y. Li, Z. Jiang, C. Liu, J. Zhang, X. Zhou, B. Hu, J. Chen, H. Hu, D. Wang, Y. Zhang, Y. Liu, Z. Liu, X. Wang, B. Xu, *ACS Energy Lett.* **2023**, *8*, 637.
[6] a) H. Lai, D. Lu, Z. Xu, N. Zheng, Z. Xie, Y. Liu, *Adv. Mater.* **2020**, *32*, 2001470; b) M. Liu, T. Pauporté, *Nano-Micro Lett.* **2023**, *15*, 134.
[7] J. Park, J. Kim, H.-S. Yun, M. J. Paik, E. Noh, H. J. Mun, M. G. Kim, T. J. Shin, S. I. Seok, *Nature* **2023**, *616*, 724.
[8] W. Zhang, X. Wu, J. Zhou, B. Han, X. Liu, Y. Zhang, H. Zhou, *ACS Energy Lett.* **2022**, *7*, 1842.
[9] a) R. Wang, X. Dong, Q. Ling, Q. Fu, Z. Hu, Z. Xu, H. Zhang, Q. Li, Y. Liu, *ACS Energy Lett.* **2022**, *7*, 3656; b) S. Wu, J. Zhang, Z. Li, D. Liu, M. Qin, *Joule* **2020**, *4*, 1248.
[10] a) W. Yan, S. Ye, Y. Li, W. Sun, H. Rao, Z. Liu, Z. Bian, C. Huang, *Adv. Energy Mater.* **2016**, *6*, 1600474; b) J. Yang, C. Liu, C. Cai, X. Hu, Z. Huang, *Adv. Energy Mater.* **2019**, *9*, 1900198; c) J.-W. Lee, S.-H. Bae, Y.-T. Hsieh, N. De Marco, M. Wang, P. Sun, Y. Yang, *Chem* **2017**, *3*, 290.
[11] A. Maiti, A. J. Pal, *J. Phys. Chem. Lett.* **2022**, *13*, 9875.
[12] a) D. Li, Z. Xing, L. Huang, X. Meng, X. Hu, T. Hu, Y. Chen, *Adv. Mater.* **2021**, *33*, 2101823; b) X. Zhang, G. Wu, W. Fu, M. Qin, W. Yang, J. Yan, Z. Zhang, X. Lu, H. Chen, *Adv. Energy Mater.* **2018**, *8*, 1702498.
[13] M. Shao, T. Bie, L. Yang, Y. Gao, X. Jin, F. He, N. Zheng, Y. Yu, X. Zhang, *Adv. Mater.* **2021**, *34*, 2107211.
[14] D. H. Cao, C. C. Stoumpos, O. K. Farha, J. T. Hupp, M. G. Kanatzidis, *J. Am. Chem. Soc.* **2015**, *137*, 7843.
[15] A. K. Jena, A. Kulkarni, T. Miyasaka, *Chem. Rev.* **2019**, *119*, 3036.
[16] I. C. Smith, E. T. Hoke, D. Solis-Ibarra, M. D. Mcgehee, H. I. Karunadasa, *Angew. Chem., Int. Ed.* **2014**, *53*, 11232.

© 2023 The Authors. Advanced Materials Interfaces published by Wiley-VCH GmbH

21967350, 2024, 6, Downloaded from https://onlinelibrary.wiley.com/doi/10.1002/admi.202300773 by HONG KONG POLYTECHNIC UNIVERSITY HUNG HOM, Wiley Online Library on [26/11/2024]. See the Terms and Conditions (https://onlinelibrary.wiley.com/terms-and-conditions) on Wiley Online Library for rules of use; OA articles are governed by the applicable Creative Commons License

[17] J. V. Milic, S. M. Zakeeruddin, M. Grätzel, *Acc. Chem. Res.* **2021**, *54*, 2729.
[18] S. Macpherson, T. A. S. Doherty, A. J. Winchester, S. Kosar, D. N. Johnstone, Y.-H. Chiang, K. Galkowski, M. Anaya, K. Frohna, A. N. Iqbal, S. Nagane, B. Roose, Z. Andaji-Garmaroudi, K. W. P. Orr, J. E. Parker, P. A. Midgley, K. M. Dani, S. D. Stranks, *Nature* **2022**, *607*, 294.
[19] M. Kim, G.-H. Kim, T. K. Lee, I. W. Choi, H. W. Choi, Y. Jo, Y. J. Yoon, J. W. Kim, J. Lee, D. Huh, H. Lee, S. K. Kwak, J. Y. Kim, D. S. Kim, *Joule* **2019**, *3*, 2179.
[20] J. Lu, T. Yang, T. Niu, N. Bu, Y. Zhang, S. Wang, J. Fang, X. Chang, T. Luo, J. Wen, Y. Yang, Z. Ding, K. Zhao, S. Liu, *Energy Environ. Sci.* **2022**, *15*, 1144.
[21] H. Zhong, X. Liu, M. Liu, S. Yin, Z. Jia, G. Fu, S. Yang, W. Kong, *Nano Energy* **2023**, *105*, 108014.
[22] a) H. Tsai, W. Nie, J.-C. Blancon, C. C. Stoumpos, R. Asadpour, B. Harutyunyan, A. J. Neukirch, R. Verduzco, J. J. Crochet, S. Tretiak, L. Pedesseau, J. Even, M. A. Alam, G. Gupta, J. Lou, P. M. Ajayan, M. J. Bedzyk, M. G. Kanatzidis, A. D. Mohite, *Nature* **2016**, *536*, 312; b) F. Huang, P. Siffalovic, B. Li, S. Yang, L. Zhang, P. Nadazdy, G. Cao, J. Tian, *Chem. Eng. J.* **2020**, *394*, 124959.
[23] H. Peng, D. Li, Z. Li, Z. Xing, X. Hu, T. Hu, Y. Chen, *Nano-Micro Lett.* **2023**, *15*, 91.
[24] X. Lian, J. Chen, M. Qin, Y. Zhang, S. Tian, X. Lu, G. Wu, H. Chen, *Angew. Chem., Int. Ed.* **2019**, *58*, 9409.
[25] a) Z. Wang, Q. Wei, X. Liu, L. Liu, X. Tang, J. Guo, S. Ren, G. Xing, D. Zhao, Y. Zheng, *Adv. Funct. Mater.* **2021**, *31*, 2008404; b) Y. Lin, Y. Fang, J. Zhao, Y. Shao, S. J. Stuard, M. M. Nahid, H. Ade, Q. Wang, J. E. Shield, N. Zhou, A. M. Moran, J. Huang, *Nat. Commun.* **2019**, *10*, 1008; c) G. Wu, X. Li, J. Zhou, J. Zhang, X. Zhang, X. Leng, P. Wang, M. Chen, D. Zhang, K. Zhao, S. Liu, H. Zhou, Y. Zhang, *Adv. Mater.* **2019**, *31*, 1903889.
[26] a) D. P. Mcmeekin, Z. Wang, W. Rehman, F. Pulvirenti, J. B. Patel, N. K. Noel, M. B. Johnston, S. R. Marder, L. M. Herz, H. J. Snaith, *Adv. Mater.* **2017**, *29*, 1607039; b) D. Ghosh, P. Walsh Atkins, M. S. Islam, A. B. Walker, C. Eames, *ACS Energy Lett.* **2017**, *2*, 2424.
[27] H. Tsai, R. Asadpour, J. C. Blancon, C. C. Stoumpos, J. Even, P. M. Ajayan, M. G. Kanatzidis, M. A. Alam, A. D. Mohite, W. Nie, *Nat. Commun.* **2018**, *9*, 2254.
[28] C. Han, Y. Wang, J. Yuan, J. Sun, X. Zhang, C. Cazorla, X. Wu, Z. Wu, J. Shi, J. Guo, H. Huang, L. Hu, X. Liu, H. Y. Woo, J. Yuan, W. Ma, *Angew. Chem., Int. Ed.* **2022**, *61*, e202205111.
[29] D. Zheng, F. Raffin, P. Volovitch, T. Pauporté, *Nat. Commun.* **2022**, *13*, 6655.
[30] a) D. Zheng, C. Schwob, Y. Prado, Z. Ouzit, L. Coolen, T. Pauporté, *Nano Energy* **2022**, *94*, 106934; b) D. Zheng, P. Volovitch, T. Pauporté, *Small Methods* **2022**, *6*, e2200633.
[31] D. Zheng, T. Zhu, Y. Yan, T. Pauporté, *Adv. Energy Mater.* **2022**, *12*, 2103618.
[32] H.-L. Loi, J. Cao, X. Guo, C.-K. Liu, N. Wang, J. Song, G. Tang, Y. Zhu, F. Yan, *Adv. Sci.* **2020**, *7*, 2000776.
[33] Y. Liu, R. Lu, J. Zhang, X. Guo, C. Li, *J. Mater. Chem. A* **2021**, *9*, 26086.
[34] C.-H. Chen, C.-C. Lin, C.-H. Chiang, C.-Y. Lin, K. Tsukagoshi, C.-W. Chen, Y. P. Chiu, S.-F. Tsay, Y.-C. Wang, *Nano Energy* **2021**, *89*, 106362.
[35] R. Ollearo, A. Caiazzo, J. Li, M. Fattori, A. J. J. M. Van Breemen, M. M. Wienk, G. H. Gelinck, R. A. J. Janssen, *Adv. Mater.* **2022**, *34*, 2205261.
[36] H. Zheng, G. Liu, L. Zhu, J. Ye, X. Zhang, A. Alsaedi, T. Hayat, X. Pan, S. Dai, *Adv. Energy Mater.* **2018**, *8*, 1800051;
[37] Y. Kusumawati, M. A. Martoprawiro, T. Pauporté, *J. Phys. Chem. C* **2014**, *118*, 9974.

© 2023 The Authors. Advanced Materials Interfaces published by Wiley-VCH GmbH

21967350, 2024, 6, Downloaded from https://onlinelibrary.wiley.com/doi/10.1002/admi.202300773 by HONG KONG POLYTECHNIC UNIVERSITY HUNG HOM, Wiley Online Library on [26/11/2024]. See the Terms and Conditions (https://onlinelibrary.wiley.com/terms-and-conditions) on Wiley Online Library for rules of use; OA articles are governed by the applicable Creative Commons License